THE JOURNAL OF PHYSICAL CHEMISTRY B
A JOURNAL OF THE AMERICAN CHEMICAL SOCIETY

Water Dynamics in Composite Aqueous Suspensions of Cellulose Nanocrystals and a Clay Mineral Studied through Magnetic Resonance Relaxometry

Anant Kumar,* Carlos Cruz, João L. Figueirinhas, Pedro J. Sebastião, Ana C. Trindade, Susete N. Fernandes, Maria H. Godinho, and Jon Otto Fossum

Cite This: https://doi.org/10.1021/acs.jpcb.1c07331 Read Online

ABSTRACT: ^{1}H spin−lattice relaxation time (T_1) measurements were performed to probe the dynamic behavior of water in aqueous suspensions of cellulose nanocrystals (CNCs) and a layered smectite clay mineral with different degrees of concentration. ^{1}H−T_1 experiments were carried out over a wide frequency domain, ranging from a few kilohertz to 500 MHz, with the aid of conventional and fast field cycling nuclear magnetic resonance (NMR) techniques. The experimental relaxometry data illustrate differences between the dynamic behavior of bulk water and that confined in the vicinity of CNC−clay surfaces. Clay alone in moderate concentration was found to enforce almost no effect on the water dynamics, whereas introducing CNCs to the system presented a significantly enhanced relaxivity. The modeling of the relaxation dispersions allowed the determination of dynamical processes and variables explaining the dynamic behavior of water in CNC−clay suspensions. It turned out that reorientations mediated by translational displacements are a leading NMR relaxation mechanism for water interacting with the surfaces of CNC−clay particles in the low-frequency domain. In the high-frequency regime, however, the inner-sphere paramagnetic relaxation mechanism dominates, which is caused by the interaction of water protons with dissolved Fe ions.

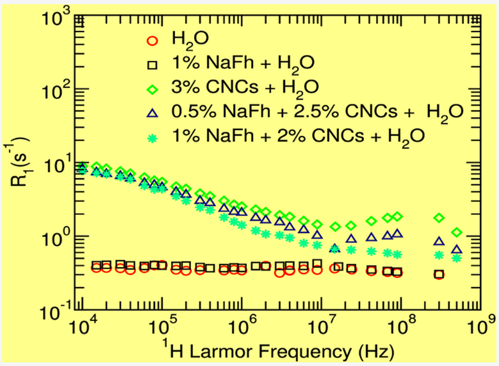

■ INTRODUCTION

With the increasing demand for environment-friendly renewable materials, nanocomposites have become a subject of intense investigation.[1−5] Nanocomposites are a group of hybrid materials resulting from the combination of naturally occurring polymers and inorganic nanosized particles. Nanocomposites offer excellent advantages in developing functional materials with desired chemical, physical, and mechanical properties, depending on the applicability.[3,4] Incorporating nanoparticles into a polymer network is a leading technique to achieve or control the properties of composite materials.[3] The properties of nanocomposite materials depend not only on the properties of the constituting parent components but also on their morphology and interfacial characteristics.[4] The substantial property enhancements displayed by nanocomposites makes them an important class of materials offering a wide range of applications.[4] Among the various nanocomposites, polymer−clay nanocomposites have attracted increasing attention in recent times because of the existence of novel properties that differ from their virgin counterparts.[5] Polymer−clay nanocomposites have been reported since the 1960s;[6,7] however, they gained attention only in the early 1990s when the central research laboratory of Toyota prepared a nanocomposite of nylon-6 with montmorillonite clay, demonstrating significant improvements in the thermal and mechanical properties.[8]

Using biodegradable polymers for nanocomposites may lead not only to the development of new materials with desirable properties but also, in particular, to the replacement of nonrenewable polymers. There are many types of biodegradable polymers that have been used to produce nanocomposite materials such as cellulose, chitosan, polylactide, gelatin, and poly(3-hydroxy butyrate).[9] Among them, cellulose is low-cost, renewable, biodegradable, and the most abundant naturally occurring organic polymer on earth and is widely available in plants. The primary source of cellulose is wood pulp and cotton. Cellulose is a linear polymer made of glucose subunits held together by β-1,4 bonds. van der Waals and intermolecular hydrogen bonds between hydroxyl groups and the oxygen of adjacent molecules are known to be responsible

Received: August 18, 2021
Revised: October 22, 2021

for the parallel stacking of cellulose chains.[10] These bundles of parallell-oriented molecules aggregate into microfibrils. Within these cellulose chains, there are highly ordered domains (crystalline) interseparated by disordered (amorphous) regions with varying degrees of crystallinity, depending on the source of cellulose.[11] However, these crystalline regions can be extracted from cellulose microfibrils through a combined chemical and mechanical treatment, producing cellulose nanocrystals (CNCs). In contrast with bulk cellulose, which exhibits a larger amount of amorphous region, CNCs have significantly enhanced mechanical strength, a uniform nanorod shape, high surface area, and unique liquid crystalline character.[12] CNCs in water, at a given concentration, have shown the ability to self-organize into a chiral nematic (cholesteric) liquid-crystalline phase with a helical arrangement.[13,14] Because of this remarkable feature, the dried films of aqueous CNCs suspensions can produce structural colors,[15] a fascinating feature of certain surfaces, mostly found in nature, that change color with illumination or by changing the viewing angle.[16] These structural colors can be tuned, over a broad range, by controlling the pitch of the chiral nematic structure and also by modifying the preparation conditions of CNCs.[14,17] CNCs also exhibit many more outstanding properties that are potentially useful for many industrial applications, such as textiles, optics, composite materials, aviation, pharmaceuticals, and health care.[18]

A broad variety of nanoparticles, such as clays, carbon nanotubes, and graphene[19] have been reported to be used in the formation of nanocomposites with different polymers. The properties of a polymer nanocomposite largely depend on the properties of incorporated nanoparticles, namely, their shape, size, aspect ratio, specific surface area, and so on.[20] Among all kinds of nanoparticles, clays have been found to be effective because of their wide availability, cost-effectiveness, and easy processability.[21] In particular, the smectite-type clays are known to form nematic liquid-crystalline phases in aqueous suspensions.[22,23] Clay-based nanocomposites have been exceedingly studied and explored to find a wide range of applications, such as adsorbents of organic pollutants in water, soils, and air, rheological modifiers in paints, inks, and grease, and drug delivery carriers.[24] It has been observed that the addition of clay can substantially improve the mechanical and thermal properties of nanocomposites.[25] The smectite-type clays, such as montmorillonite and fluorohectorite, are the most used clays in the synthesis of polymer nanocomposites. They are characterized by a layered structure with a layer thickness in the nanometer range. It is a fact that the dried films of CNCs can generate structural colors, whereas nanoclays are reported to be used as rheological modifiers.[26] Hence the CNC−clay composites have opened a new horizon for researchers to develop new, environment-friendly, multifunctional surfaces and coatings for the coloration and reflection of light. In such structurally colored materials, the reflected colors can be tuned by controlling the concentration of added CNCs.

In conjunction with many key features, understanding the complex interaction between polymer−clay nanocomposites and their solvents is equally important in determining the overall material properties.[27,28] The structure and dynamics of water are assumed to be modified when water molecules are confined in nanoscale cavities or are close to interfaces. Understanding the dynamic properties of such confined water might reveal many microscopic details regarding the interfacial relationship between the confined water and the confining environment. In this context, a detailed analysis of the influence of the polymer/clay composition on the structural and dynamic properties of solvent water is of prime importance. However, there are not many studies probing the dynamic properties of water in polymer/clay nanocomposites. In this work, motivated by the potential applications demonstrated by these multifunctional materials and the insight that NMR techniques can unveil, we have investigated, by pulsed-field-gradient (PFG) NMR and ^{1}H NMR relaxometry, the dynamic behavior of water in aqueous suspensions of CNCs and sodium-fluorohectorite clay (CNC−NaFh) at different concentrations. Among the large body of experimental techniques, ^{1}H NMR relaxometry provides a unique tool to study water dynamics in a confined environment and conclude on possible interaction mechanisms. PFG-NMR provides a direct means for obtaining information on the translational diffusion of nuclear spins.

The spin−lattice relaxation time, T_1 (reciprocal of the relaxation rate, R_1) reflects the recovery rate at which the longitudinal component of the magnetization vector recovers toward its thermodynamic equilibrium, and it is affected by many factors such as the solvent, temperature, nuclear environment, and molecular motions. Therefore, the proton NMR relaxometry, being very sensitive to host−water interactions, could serve as a highly suited method for the identification and characterization of water dynamics in restricted geometries imposed by the added CNC−clay complexes on a variety of time scales. The spin−lattice relaxation rate of protons is usually driven by fluctuating dipole−dipole interactions. It is consequently composed of intramolecular and intermolecular contributions. The intramolecular relaxation process is governed by rotation/reorientation motions, whereas the intermolecular contribution includes the self-diffusion mechanism. In addition, there are more specific contributions that are often included to fully account for the relevant relaxation mechanisms. These contributions, in the nuclear magnetic relaxation dispersion (NMRD) curves of R_1, dominate in different frequency ranges and therefore can be identified and separated. Many relaxation models are available to fit the NMRD curves, which allow us to separate different contributions to R_1 arising from different molecular motions depending on the frequency tested. The analysis of NMRD profiles based on such relaxation models enables the evaluation of various molecular parameters and interprets how they influence the relaxation behavior. On the basis of these interpretations, we can discriminate the dynamic behavior of both bulk water and water in aqueous suspensions at different CNCs/clay concentrations. Indeed, being new systems to the NMR relaxometry, they present a new challenge on the choice of appropriate models to understand the shape of relaxation profiles and on extracting meaningful motional parameters (e.g., motional correlation times) that are important for explaining the dynamic relations and internal interactions between water molecules and their environment.

Through the presented study, we will provide detailed knowledge on the interactions of CNC−clay surfaces with solvent water that might contribute to the development of new materials with targeted properties and relevant applications.

■ MATERIALS AND METHODS

Materials. In this work, aqueous suspensions of CNCs and a high-aspect-ratio sodium-fluorohectorite (NaFh) synthetic clay, dispersed in different ratios, were used to study the T_1 spin−lattice relaxation time. Sodium fluorohectorite, NaFh ($Na_{0.5}[Mg_{2.5}Li_{0.5}]Si_4O_{10}F_2$), was synthesized using a melt process according to a published procedure.[29] The NaFh particles may exhibit diameters of up to ∼200 μm, whereas their delaminated nanolayer thickness is ∼1 nm. The rod-like CNCs have dimensions between 5 and 10 nm in width, with lengths of 100−150 nm.

Preparation of Composite Aqueous Suspensions of CNCs/Clay. CNCs were produced via the sulfuric acid hydrolysis of cellulose microcrystal (CMC) that was derived from cotton (Avicel PH-101, particle size of 50 mm, Fluka), as described elsewhere.[30] The counterion H^+ of the resultant acid from CNC−H was replaced by Na^+ using a mixed-bed Amberlite IR120 Na ion-exchange resin from Aldrich and following the batch method adapted from Dong et al.[31]

CNC−clay composite suspensions were obtained by mixing a suspension of NaFh at 1.0 wt % in water with the previously mentioned CNCs suspension, giving rise to suspensions with 2.5/0.5 wt % and 2.0/1.0 wt % CNCs/NaFh. This is the same protocol as was previously used in ref 32. Fifteen mL of CNC suspension with a solid content of 3.0 wt %, as obtained, was dispersed and sonicated for 15 min with an ultrasonic probe (Dr. Hielscher UP400 St, 3 mm diameter titanium tip) with an energy input of 0.82 kJ/mL.

ICP-AES Analysis. Oven-dried samples of CNCs, CMCs, and all of the chemical compounds used in the hydrolysis process were characterized by elemental analysis (inductively coupled plasma atomic emission spectroscopy (ICP-AES)) for the presence of any metal content. The analyses were carried out on a Horiba Jobin-Yvon ULTIMA sequential ICP apparatus through the Horiba Jobin-Yvon ICP Analyst 5.4 software using a monochromator with a Czerny−Turner spectrometer.

ICP-AES analyses revealed a sulfur content of 0.97 wt %, equivalent to 5-OSO3-Na^+/100 anhydroglucose units, according to the $C_6H_{10}O_5-(SO_3)$ formula and calculated from the equation $S\,(\%) = 100n \times S/[6C + 10H + (5 + 3n)O + nS]$.[33] A value of 1.01 wt % was determined for Na through these analyses.

^{1}H NMR Relaxometry. The ^{1}H spin−lattice relaxation times (T_1) of the water in the bulk and confined states were measured at 25 °C across a broad frequency range from a few kilohertz to 500 MHz. We covered such a broad frequency range with three different spectrometers using two different techniques. Bruker 7 and 11.7 T superconducting magnets, both connected to Bruker Avance II consoles, were used to measure the T_1 values at 300 and 500 MHz, respectively. In the frequency range between 10 and 100 MHz, relaxivity measurements were performed on a variable-field (0.2 to 2 T) iron-core electromagnet (BE30) also connected to the Bruker Avance II console. At lower fields from 10 kHz to 9 MHz, a home-developed fast field cycling (FFC) NMR relaxometer was employed. For frequencies higher than 10 MHz, the measurements were performed using the classical inversion−recovery technique.[34] For the frequencies below 10 MHz, the FFC technique[35] was used to obtain the relaxation data. In this technique, the ^{1}H spin system is subjected to rapid variations between different magnetic field intensities. This allows the measurement of relaxation times over a wide range of field strengths with just one instrument. In our FFC relaxometer, both the polarizing (B_P) and detection (B_D) fields are equal to 0.215 T with a switching time of <3 ms.[35] In these NMR measurements, a standard airflow system controlled the temperature with a precision of ±0.5 °C. The experimental error for the measurements of the spin−lattice relaxation time is estimated to be ∼5%. These experiments provide raw NMR relaxation data, that is, the time evolution of the longitudinal magnetization of water protons that was, to determine the T_1 values at each frequency, fitted to a monoexponential recovery function

$$M_z(t) = M_z^{\infty} + (M_z^{\circ} - M_z^{\infty})e^{(-t/T_1(\omega))} \tag{1}$$

This shows that the z-magnetization, $M_z(t)$, returns from the perturbed state, M_z°, to the equilibrium state, M_z^{∞}, following an exponential law. ω is the Larmor or precessional frequency that depends on the magnetic field experienced by the nucleus.

^{1}H NMR Diffusometry. To aid in the separation of different dynamical processes, we also carried out independent NMR diffusometry measurements in the studied systems that allow for a precise determination of the self-diffusion coefficient (D) of water molecules, fixing the parametric contribution of the self-diffusion mechanism to the relaxation rate, R_1. The D values in the studied samples were measured by applying a stimulated-eco pulsed-field gradient (STE-PFG) sequence[36] with the aid of a 7T Bruker Avance III console (operating at ^{1}H resonance frequency 300 MHz) equipped with a Bruker Diff30 diffusion probe and a magnetic field gradient unit. Owing to the stream of compressed air, the sample temperature of 25 °C was controlled throughout the measurement within an uncertainty of ±0.5 °C. In these experiments, the attenuation of the NMR signal intensity (due to molecular diffusion) is measured as a function of the strength of the applied magnetic field gradient, keeping all other sequence parameters constant. This intensity change is described according to the following equation[37,38]

$$I(g) = I_o \exp\left[-D\gamma_H^2 g^2 \delta^2\left(\Delta - \frac{\delta}{3}\right)\right] \tag{2}$$

For one of the studied samples, however, a biexponential decay of the magnetization was observed; therefore, two diffusion coefficients (D_I and D_{II}) were estimated. One is associated with the water moving in bulk with a relative population q, and the other is associated with the water in contact with the CNC-NaFh surfaces, with a relative population $(1 - q)$. In that case, the model fitting expression takes the following form

$$I(g) = qI_o \exp\left[-D_I\gamma_H^2 g^2 \delta^2\left(\Delta - \frac{\delta}{3}\right)\right] + (1 - q)I_o \exp\left[-D_{II}\gamma_H^2 g^2 \delta^2\left(\Delta - \frac{\delta}{3}\right)\right] \tag{3}$$

In these equations, I is the observed intensity, I_0 represents the reference intensity in the absence of a gradient, D is the diffusion coefficient, γ_H is the gyromagnetic ratio of the proton, Δ is the diffusion time, g is the amplitude of the gradient pulse, and δ is the length of the gradient pulse. It follows that by incrementing g over a range of values, the observed attenuation data of $I(g)$ can be fitted to eq 2 or 3 to extract the diffusion coefficients of the spin-bearing molecules.

Data Analysis. The experimental ^{1}H NMRD profiles over the complete frequency range (10 kHz to 500 MHz), obtained by combining the R_1 values measured through all three spectrometers, were analyzed by using the least-squares minimization procedure, as implemented in an online fitting platform, fitteia.org.[39] *fitteia* is a web-based application that allows the dispersion profiles to be fit in terms of various relaxation modes to distinguish different dynamic processes.

■ THEORETICAL BACKGROUND

The spin−lattice relaxation is a stimulated process induced by the fluctuations of the local magnetic field from neighboring spins. Hence any process that causes such fluctuations can be considered as a possible relaxation mechanism. Usually, there is a coexistence of many of these relaxation mechanisms. However, assuming that different molecular motions are statistically independent or have considerably different characteristics time scales, any cross-relaxation contribution is neglected. In such a case, the frequency dependence of the overall spin−lattice relaxation rate R_1 ($= 1/T_1$) can be expressed by the superposition of different relaxation mechanisms $(R_1)_i$, each one associated with a specific type of molecular motion

$$R_1(\omega) = \frac{1}{T_1(\omega)} = \sum_{i=1}^{n} \frac{1}{T_{1,i}(\omega)}$$

Here i represents the contribution of individual molecular motions to the spin−lattice relaxation rate. The individual motions considered in this work are molecular rotations/reorientations (ROT), translational self-diffusion (SD), paramagnetic relaxation (PAR), and rotations mediated by translational displacements (RMTD). Thus, for the overall relaxation rate, we can write

$$\frac{1}{T_1} = \left(\frac{1}{T_1}\right)_{\mathrm{ROT}} + \left(\frac{1}{T_1}\right)_{\mathrm{SD}} + \left(\frac{1}{T_1}\right)_{\mathrm{PAR}} + \left(\frac{1}{T_1}\right)_{\mathrm{RMTD}} \tag{4}$$

Molecular Rotations/Reorientations. To describe rotations, we used the well-known Bloemberg−Purcell−Pound (also known as BPP) theory[40] involving a single correlation time to describe the isotropic rotations. According to this theory, the frequency dependence of the relaxation rate can be expressed as

$$\left(\frac{1}{T_1}\right)_{\mathrm{ROT}} = A_{\mathrm{ROT}}\left(\frac{\tau_c}{1 + \omega^2\tau_c^2} + \frac{4\tau_c}{1 + 4\omega^2\tau_c^2}\right) \tag{5}$$

with the prefactor $A_{\mathrm{ROT}} = 3\mu_o^2\gamma^4\hbar^2/160\pi^2 < r_{ij}^6 >$, where τ_c is the correlation time that can be replaced by the rotational correlation time because, in this situation, the relaxation is dominated by rotations. The rotational correlation time is the average time interval between rotations of nuclei or the time it takes for the nucleus to diffuse or rotate into a nearby position. ω is the Larmor frequency, which depends on the type of the nucleus and the strength of the applied magnetic field. μ_o is the magnetic permeability of free space, γ is the gyromagnetic ratio of the nucleus under investigation, $\hbar$ is the reduced Planck constant, and r_{ij} is the distance between spin nuclei. <> represents an ensemble average performed over all spin−pair distances.

Translational Self-Diffusion. Relaxation due to translational diffusion or self-diffusion is a mechanism by which spin relaxation occurs through the modulation of dipole−dipole interactions between protons located on different molecules. The relaxation rate contribution associated with translational self-diffusion (SD) has been analyzed based on Torrey's model.[41] Torrey's model was devised from the BPP model to address the relaxation due to diffusion. Torrey's model assumes equally probable jumps of molecules in any random direction to the neighboring sites from an initial one. According to Torrey's model, we can write the relaxation rate as

$$\left(\frac{1}{T_1}\right)_{\mathrm{SD}} = A_{\mathrm{SD}}[\zeta(\omega\tau_{\mathrm{SD}}) + 4\zeta(2\omega\tau_{\mathrm{SD}})] \tag{6}$$

with prefactor $A_{\mathrm{SD}} = (N_{\mathrm{H}}\tau_{\mathrm{SD}}/2d^3)({}^{3\mu_o\gamma_{\mathrm{H}}^2\hbar}\!/_{8\pi})^2$. Here $\zeta(\omega\tau_{\mathrm{SD}})$ is a dimensionless analytical function that depends on the average time between diffusion jumps (τ_{SD}), the mean square of the jump length ($\langle r^2\rangle$), and the lateral distance between neighboring molecules (the distance of closest approach), d. The correlation time (τ_{SD}) is related to the translational diffusion constant (D) through the expression $\langle r^2\rangle = 6\tau_{\mathrm{SD}}D$. N_{H} is the number of ^{1}H spins per unit volume.

Paramagnetic Relaxation. Brownian motion of a paramagnetic species/ion induces a fluctuating magnetic field that promotes relaxation in nearby solvent molecules. The paramagnetic relaxation originates from the dipole−dipole interaction between the investigated nuclear spins and the fluctuating local magnetic field, resulting from unpaired electron spins of paramagnetic species, including iron, manganese, and molecular/dissolved oxygen. If the frequency of these fluctuations has a component at or near the Larmor frequency, then a significant enhancement of proton relaxation is induced. When the solvent molecules (mostly water) approach a paramagnetic center, magnetic interactions between water protons and paramagnetic centers speed up the relaxation of water protons to their magnetic equilibrium. Typically, the relaxation of water protons in the close vicinity of paramagnetic entities could be classified into two regions of interactions: the inner sphere (IS) and the outer sphere (OS). The IS relaxation contribution originates from the direct coordination (temporary binding) of water molecules to paramagnetic centers, and when these water molecules exchange with bulk water molecules, the paramagnetic effect propagates to the entire solvent surrounding the paramagnetic entity. OS relaxation is a more complex mechanism. Solvent molecules of the bulk, which are not directly bound to the paramagnetic species but diffusing around them, also experience the paramagnetic effect. This relaxation contribution represents the OS (purely diffusive) relaxation.

A combined paramagnetic relaxation rate enhancement due to the paramagnetic agent is therefore given by

$$\left(\frac{1}{T_1}\right)_{\mathrm{PM}} = \left(\frac{1}{T_1}\right)_{\mathrm{IS}} + \left(\frac{1}{T_1}\right)_{\mathrm{OS}} \tag{7}$$

where the subscripts "IS" and "OS" stand for the inner- and outer-sphere relaxations, respectively.

Inner-Sphere Relaxation. The IS contribution to the overall relaxation rate is given by

$$\left(\frac{1}{T_1}\right)_{\mathrm{IS}} = \frac{cq}{55.5}\frac{1}{(T_{1\mathrm{m}} + \tau_{\mathrm{m}})} \tag{8}$$

where c is the molar concentration of paramagnetic species, q is the number of IS solvent molecules simultaneously bonded to each paramagnetic particle, τ_{m} is the average time a bonded solvent molecule spends in the IS of the paramagnetic site (equal to the reciprocal of the solvent molecule exchange rate between its bound-state and the in-bulk state), and T_{1m} is the relaxation time of the protons of solvent molecules in the IS or bound state.

On the basis of Solomon–Bloembergen–Morgan equations of paramagnetic relaxation theory,[42−44] the relaxation rate of bound solvent protons ($1/T_{1m}$) can be expressed in terms of two components arising from dipole–dipole ("through-space") and scaler (contact or "through-bond") interactions. Because the relaxation rates are additive, $1/T_{1m}$ can be written as

$$\frac{1}{T_{1m}} = \left(\frac{1}{T_1}\right)_{DD} + \left(\frac{1}{T_1}\right)_{SC}$$

The individual relaxation terms are given as

$$\left(\frac{1}{T_1}\right)_{DD} = \frac{2}{15}\left(\frac{\mu_o}{4\pi}\right)^2 \frac{\hbar^2\gamma_H^2 g_e^2 \mu_B^2}{r_{MH}^6} S(S+1)\left[\frac{3\tau_{d1}}{1+\omega_H^2\tau_{d1}^2} + \frac{7\tau_{d2}}{1+\omega_S^2\tau_{d2}^2}\right]$$

$$\left(\frac{1}{T_1}\right)_{SC} = \frac{2}{3}\left(\frac{A}{\hbar}\right)^2 S(S+1)\left[\frac{\tau_{SC}}{1+\omega_S^2\tau_{SC}^2}\right]$$

Here S is the total electronic spin of metal ion, γ_H is the gyromagnetic ratio of the proton, g_e is the electronic g-factor, μ_B is the Bohr magneton, r_{MH} is the proton–metal ion distance, ω_H and ω_S are the Larmor frequencies of the proton and electron, respectively, and $(A/\hbar)$ is the hyperfine or SC coupling constant between the electron spin of the paramagnetic center and the proton spin of the bound solvent. For most paramagnetic ions, the interaction with solvent protons is through space, so the dipolar mechanism dominates the $1/T_{1m}$ relaxation.[45] The correlation times appearing in these equations describe the time fluctuations of the corresponding interactions and can have contributions from different mechanisms.[46] The overall correlation times, corresponding to the dipolar, τ_d, and scalar, τ_{SC}, relaxations, are defined as

$$\frac{1}{\tau_d} = \frac{1}{T_{1e}} + \frac{1}{\tau_m} + \frac{1}{\tau_R}$$

$$\frac{1}{\tau_{SC}} = \frac{1}{T_{1e}} + \frac{1}{\tau_m}$$

Here T_{1e} stands for the longitudinal electronic relaxation times of the paramagnetic ion, τ_m is the residence lifetime of a solvent molecule in the inner sphere, and $\tau_d = 1/(6D_R)$ is the rotational correlation time of the entire metal–water complex, with D_R as the rotational diffusion coefficient.

Like other relaxation processes, electronic relaxation rates also depend on the magnetic field. For metal ions with spin $S >$ 1/2, there is zero-field splitting (ZFS) of electronic energy levels. Compared with microscopic parameters such as molecular rotations and vibrations, the ZFS interactions are the primary cause of electronic relaxation.[46] On the basis of the Bloembergen–Morgan theory[42−44] the modulation of electronic relaxation rates through ZFS can be described by the following equations

$$\left(\frac{1}{T_{1e}}\right)_{ZFS} = \frac{1}{25}\Delta^2\tau_V\{4S(S+1)-3\}\left[\frac{1}{1+\omega_S^2\tau_V^2} + \frac{4}{1+4\omega_S^2\tau_V^2}\right]$$

Here Δ^2 represents the mean-squared amplitude of the ZFS in frequency units, and τ_v is the correlation time for the modulation of the ZFS. When combined, these equations establish a complete theory for the description of the paramagnetic relaxation rate enhancement, and it is referred to as the Solomon–Bloembergen–Morgan theory.[42−44] A complete description of this theory can be found in the literature.

Outer-Sphere Relaxation. In a limiting case when the paramagnetic species weakly interact with the nuclear spins of solvent molecules (i.e., τ_m becomes very short), the contribution of the ion–nucleus interaction (through direct binding) may become substantially small in determining $1/T_{1m}$. Under these conditions, the OS relaxation is assumed to be purely diffusive and is described by the complex dynamics of solvent molecules and the paramagnetic species diffusing and rotating in each other's neighborhoods. The OS contribution to the paramagnetic relaxation is described by a purely diffusive model[47,48]

$$\begin{aligned}\left(\frac{1}{T_1}\right)_{OS} &= \frac{32\pi}{405}\left(\frac{\mu_o}{4\pi}\right)^2 \gamma_H^2\gamma_S^2\hbar^2\left(\frac{mN_A}{aD}\right)S(S+1)[3J_{OS}(\omega_H)+3J_{OS}(\omega_S)]\\ J_{OS}(\omega_{H/S}) &= \mathrm{Re}\left\{\frac{1+z/4}{1+z+4z^2/9+z^3/9}\right\}\\ z &= (i\omega_{H/S}\tau_D+\tau_D/T_{ie})^{1/2}\\ \tau_D &= a^2/D\end{aligned} \tag{9}$$

Here N_A is the Avogadro number, a is the distance of closest approach between the nuclear spin and electron spins, m is the molar concentration of electron spins, γ_H and γ_S are the gyromagnetic ratios of the proton and electron, respectively, τ_D is the diffusion correlation time, and D is the sum of the diffusion constants of the OS solvent molecules (bearing the proton nuclear spin) and the paramagnetic complex (bearing the electron spin), $D = D_H + D_S$. Because the solvent molecules (in the case of water) move much faster than the relatively large paramagnetic complexes, D is dominated by the self-diffusion coefficient of water.

Reorientations Mediated by Translational Displacements. In a system where small molecules are confined in nanosize cavities, molecular dynamics becomes more complex as molecular motions are restricted by the confining walls/surfaces. Near surfaces, the adsorbate molecules are expected to exhibit significantly different rotational and translational diffusion behavior in contrast with the bulk. In this mechanism, an adsorbate molecule diffusing along curved surfaces adopts a preferential orientation imposed by the surface. This orientation changes when the molecule diffuses back to the bulk (desorption). This cyclic process of adsorption, bulk diffusion, and readsorption keeps on reorienting the molecule. Hence we can say that the molecular reorientations are no longer independent of translational diffusions. Such a dynamical process in which molecular reorientations are induced by the translational displacements of molecules is known as reorientations mediated by translational displacements (RMTD), and a specific relaxation contribution (a combination of both motions) should be used in such a case. These motions are known as "slow dynamics" because they occur on a much slower time scale than bulk rotational or translational diffusion. The RMTD model, which is relevant for several confining systems, was proposed by Kimmich and coworkers.[49,50] The following equation can express the contribution of the RMTD mechanism to the overall spin−lattice relaxation

$$\left(\frac{1}{T_1}\right)_{\mathrm{RMTD}} = A_{\mathrm{RMTD}}\left\{\frac{1}{\omega^p}\int_{z_{\min}}^{z_{\max}}\frac{z^{3-2p}}{1+z^4}\,\mathrm{d}z+\frac{1}{(2\omega)^p}\int_{z_{\min}/\sqrt{2}}^{z_{\max}/\sqrt{2}}\frac{z^{3-2p}}{1+z^4}\,\mathrm{d}z\right\} \tag{10}$$

Here A_{RMTD} is the prefactor that depends on the residual dipole−dipole interactions among proton spins that are averaged by local molecular reorientations of adsorbed molecules, microstructural features of the confined matrix, the diffusion coefficient, and the fraction of molecules at the surface.[51] The exponent $p = (1 + \chi)$, with χ being the orientational structure factor varying between 0 and 1,[52] $z_{\min} = (\omega_{\mathrm{RMTD;min}}/\omega)^{1/2}$, and $z_{\max} = (\omega_{\mathrm{RMTD;max}}/\omega)^{1/2}$. The frequencies $\omega_{\mathrm{RMTD;min}}$ and $\omega_{\mathrm{RMTD;max}}$ denote the low and the high cutoff limits, respectively, which are related to the two-dimensional surface diffusion through the following relations, $\omega_{\mathrm{RMTD;min}}^{-1} = l_{\max}^2/4D_s$ and $\omega_{\mathrm{RMTD;max}}^{-1} = l_{\min}^2/4D_s$, where $l_{\min}$ and $l_{\max}$ stand for the smallest and largest displacement distances, respectively, and D_s denotes the surface diffusion coefficient.

■ RESULTS AND DISCUSSION

Determination of Diffusion Coefficients: ^{1}H NMR Diffusometry. The water diffusion coefficient (D) measured for each sample is listed in Table 1. For all of the studied samples, a monoexponential behavior of the time-dependent longitudinal magnetization was observed, except for 1% NaFh + H_2O, in which a biexponential function gave a better fitting and two diffusion coefficients were estimated. Such biexponential behavior was attributed to the existence of two distinct pools of water: (I) free water with a diffusion coefficient $D_I \approx 1.6 \times 10^{-9}$ m^2/s and (II) restricted or slowly diffusing water with a diffusion coefficient $D_{II} \approx 3.1 \times 10^{-10}$ m^2/s. The two pools of water indicated very different diffusion behaviors. Pool (I) acts much like bulk water with $b \approx 70\%$ of water population; however, for pool (II), a significantly reduced mobility was evaluated that could be associated with the diffusion of a fraction of water molecules interacting with larger partners with $(1 - b) \approx 30\%$ population. The water diffusion coefficients for the other three samples were very close to the one observed for pure water. The experimental error in the determination of diffusion constants is estimated to be within ±5%.

Table 1. Measured Values of Diffusion Constants (D) of the Studied Samples at B = 7 T and 25 °C[a]

sample	D (m^2/s)
pure H_2O	2.4 (±0.1) × 10^{-9}
1% NaFh + H_2O	D_I = 1.6 (±0.08) × 10^{-9}
	D_{II} = 3.1(±0.1) × 10^{-10}
3% CNCs + H_2O	2.2 (±0.1) × 10^{-9}
0.5% NaFh + 2.5% CNCs + H_2O	2.2 (±0.1) × 10^{-9}
1% NaFh + 2% CNCs + H_2O	2.1 (±0.1) × 10^{-9}

[a] Suspension composition in percentage values corresponds to wt %.

^{1}H NMR Relaxometry Results. The goal of NMR relaxation studies is to probe the dynamics of water that is expected to be altered in a multicomponent system due to the imposed geometrical restrictions and interfacial interactions and is reflected by changes in the NMR relaxometry data. The raw data of observed spin−lattice relaxation times of the water protons in bulk and those interacting with the CNC−NaFh surfaces are presented in Figure 1. The spin−lattice relaxation rate dispersions for the CNC-containing materials are markedly different compared with those for bulk water. It is also interesting to note that the NMRD profile of 1% NaFh + H_2O is almost identical to that of bulk water. The molecular self-diffusion measurements (see Table 1) identified two pools of water populations in this sample, although the relaxation measurements could not identify the less abundant component, probably because of its small weight percentage. A more focused analysis, however, shows that the 1% NaFh + H_2O sample has only slightly enhanced relaxivity compared with bulk water. The NMRD profiles of CNC-containing materials also exhibit relaxivity humps at high frequencies that are typical for nuclear paramagnetic relaxation mechanisms.

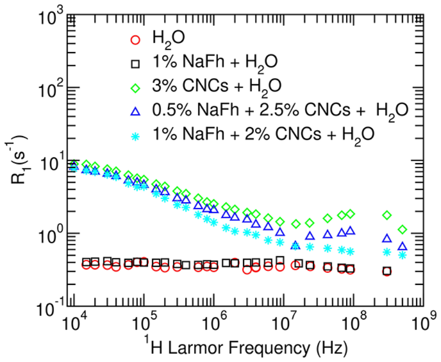

Figure 1. Frequency dependence of the proton spin−lattice relaxation times for the indicated samples observed at 25 °C.

The results depicted in Figure 1 were fitted using the model given by eq 4, which comprises different contributions to the overall relaxation mechanism, and the fitting results are presented in Figures 2 and 3. The analyses were performed by the nonlinear least-squares minimization method, as implemented in *fitteia*. The values of associated fitting parameters involved in these models are listed in Table 2. These parameters were obtained for the best fits to the experimental data while fixing their ranges within their most likely values, as reported in the literature.

The NMRD profiles for bulk H_2O and 1% NaFh + H_2O are presented in Figure 2. The observed plateaus in the NMRD curves reflect the relaxation rates that are almost independent of the Larmor frequency, as is characteristic of most conventional liquids. NMR relaxometry typically allows the detection of molecular motions with large correlation times at low frequencies; however, molecular motions with short correlation times are detected at high frequencies. The correlation times for molecular rotations, which dominate for the bulk water, are short (i.e., fast motions) throughout the studied frequency range, and thus no noticeable dispersion is observed over this range. It is expected that adding a component to water reduces its mobility compared with that

Table 2. Fitting Parameters Related to the Relaxivity of the Studied Sample Obtained from the Best Model Fit to the Experimental ^{1}H NMRD Profiles[a]

	pure H_2O	1% clay + H_2O	3% CNCs + H_2O	0.5% NaFh + 2.5% CNCs + H_2O	1.0% NaFh + 2.0% CNCs + H_2O
τ_{ROT} (10^{-12} s)	4.09	4.26	4.26	4.26	4.26
A_{RMTD} (10^2 $s^{-(1+p)}$)			3.03	3.03	3.03
τ_m (10^{-10} s)			3.91	3.91	3.91
τ_R (10^{-8} s)			6.55	6.55	6.55
Δ^2 (10^{20} s^{-2})			3.01	3.01	3.01
τ_V (10^{-12} s)			8.76	8.76	8.76
C (10^{-2} mmol/L)			11.43	3.90	0.26

[a] Suspension composition in percentage values corresponds to wt %. Parametric descriptors of hydration, r_{MH} = 3.0 Å, and q = 1, were fixed during fitting. τ_{ROT}, rotational correlation time; A_{RMTD}, prefactor for RMTD mechanism; τ_m, residence lifetime of water molecules bound to m paramagnetic centers; τ_R, rotational correlation time of the complex; Δ^2, mean-squared amplitude of the zero-field splitting; τ_V, correlation time of the zero-field splitting fluctuations; C, concentration of m paramagnetic particles.

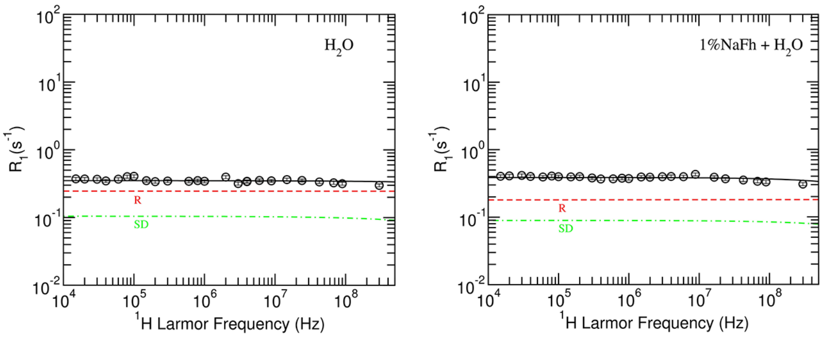

Figure 2. Experimental (circles) and fitted (solid black lines) ^{1}H NMRD profiles of bulk H_2O (left) and 1% NaFh + H_2O (right). Dashed red and green lines indicate contributions to the overall relaxation arising from molecular reorientations (R) and self-diffusion (SD), respectively.

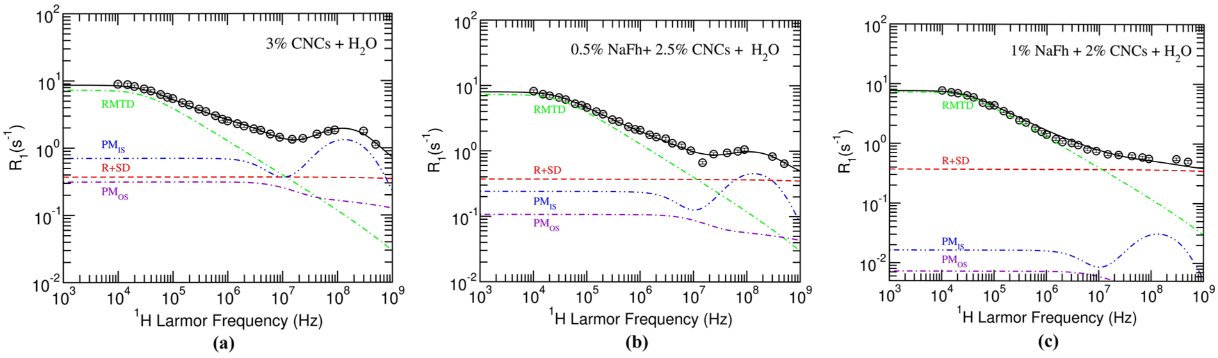

Figure 3. Experimental (circles) and fitted (solid black lines) ^{1}H NMRD profiles of (a) 3% CNCs + H_2O, (b) 0.5% NaFh + 2.5% CNCs + H_2O, and (c) 1% NaFh + 2% CNCs + H_2O. Dashed red, green, blue, and violet lines indicate contributions to the relaxation arising from molecular reorientation and self-diffusion (R + SD), reorientations mediated by translational displacements (RMTD), the paramagnetic inner-sphere (PM_{IS}), and the paramagnetic outer-sphere (PM_{OS}), respectively.

of pure water, and this effect is highly sensitive to the amount, dimensions, and chemical nature of the added component(s). However, a water-like NMRD profile is observed for 1% NaFh + H_2O. This implies that only motions with short correlation times are present in both samples, and a small concentration of NaFh clay has barely any effect on the water mobility of the observed component. The contributions of rotations (R) and self-diffusion (SD) considered in the relaxation model explain well the observed dispersions for these two samples.

In Figure 3, the R_1 dispersions for the (a) 3% CNCs + H_2O, (b) 0.5% NaFh + 2.5% CNCs + H_2O, and (c) 1% NaFh + 2% CNCs + H_2O samples are presented. It is important to note that these three samples comprise ~97 wt % water, and the mentioned ratios of CNCs and NaFh are relative to each other. For these samples, the restricted mobility of solvent (water) molecules, that is, slower dynamics, substantially influences the NMR relaxation behavior. This is also clear from the results presented in Figure 1, where, even at very low solute contents, the R_1 of CNC-interacting water is up to 18 times higher compared with that of pure water. The R_1 dispersions smoothly increase with decreasing frequency until they reach a plateau at ~10 kHz. For all three samples, the observed dispersions were not markedly different from each other, and they even overlap in the lower frequency domain. This can be because the water concentrations in these samples are almost equal (~97 wt %); therefore, the efficiency of the water–CNC/NaFh surface interaction remains very similar. Although presenting similar R_1 dispersion behavior, it is noted that the 3% CNCs + H_2O sample (without clay) has the highest relaxivity, and its magnitude decreases with an increase in the incorporation degree of added clay.

Unlike NaFh clay, introducing CNCs to pure H_2O is seen to produce a significant change in the relaxation rates of water protons by not only imparting profound enhancements of the relaxation rates in the low-frequency domain but also inducing the paramagnetic relaxation enhancement. The "bumps" observed in the NMRD profiles, in particular, for 3% CNCs + H_2O and 0.5% NaFh + 2.5% CNCs + H_2O samples, suggest the presence of paramagnetic species. These bumps are a characteristic of nuclear paramagnetic relaxation that is often observed at high frequencies. It follows that the added CNCs must have some amount of dispersed paramagnetic entity (most common are metal ions) because in the structure of CNCs, there are no paramagnetic species attached. Increasing the ratio of dissolved NaFh clay (from 0.5 to 1.0 wt %) makes it possible to further suppress the paramagnetic contribution to the overall relaxation, as can be seen in Figure 3b,c. As illustrated in Figure 2 for 1% NaFh + H_2O, there is almost no effect of NaFh clay on the relaxation behavior of water protons. Therefore, we have a sound reason to believe that the paramagnetic relaxation is induced by CNCs only, and this disappears as the concentration of NaFh clay increases; in turn, the amount of CNCs decreases. In this context, to quantify the origin of this paramagnetic-like behavior, we carried out ICP-AES analyses that allow the detection of metal elements in the samples.

ICP-AES analyses showed the presence of sulfate half-ester groups and iron (Fe) in CNCs. To determine the true source of these metals, we also conducted elemental analyses on all of the reagents that are used in the production process of CNCs. Fe was found in CMCs, in which the ICP-AES analyses returned a value of 352.6 ppm. This value is in accordance with the one found for pure CNCs, where 352.2 ppm of Fe was obtained. In the pure CNC suspension (3.0 wt %), this value corresponds to having 0.19 mmol/L of Fe, which is in close agreement with the amount estimated by NMR studies. Lower values of 0.16 and 0.13 mmol/L of Fe can be inferred for the 2.5/0.5 and 2.0/1.0 wt % of CNCs/NaFh composite suspensions, respectively. The presence of Fe in the raw material can apparently be associated with the existence of such minerals in natural cotton that depend on its maturity, type, and crop year and the inorganic fertilizers that plants absorb from the soil.

The dipole−dipole interactions between the water protons and Fe ions are therefore concluded to be responsible for the paramagnetic relaxation. As the concentration of CNCs is further decreased to 2.5 and 2.0 wt %, in turn, the molar concentration of Fe ions is reduced, and the paramagnetic relaxation enhancement is suppressed. Such paramagnetic relaxivity could originate from either or both of the IS and OS mechanisms. In this work, it was observed that the high-field bumps in the NMRD curves due to the presence of iron are well-explained by the IS mechanism, chemical exchange between bound and bulk water molecules. This also indicates that the paramagnetic centers are distributed in such a way that they are directly accessible to the water molecules; therefore, they contribute to the IS mechanism. Although the possibility of OS interactions cannot be ruled out, it seems to be insignificant.

To fit the observed NMRD profiles for the CNC-based samples, instead of including them separately, we presented the R and SD contributions by a simple curve (R + SD) with just one correlation time. The low-frequency dispersions of water molecules interacting with the internal surfaces of CNC/NaFh matrices were successfully explained by the RMTD mechanism. RMTD is the main mechanism for explaining substantially long correlation times, which can be on the order of 10^{-5} s. It is important to point out that to simplify the fitting procedure, we have kept fixed the values of those parameters that have well-known values from the literature. The distance between the Fe ion and the IS water protons (r_{MH}) was maintained at 3.0 Å. The number of water molecules coordinated in the inner coordination sphere of the Fe ion was assumed to be 1 (hydration number $q = 1$). The water residence lifetimes (τ_m), rotational correlation time of the complex (τ_{R}), mean-squared amplitude of the zero-field splitting (Δ^2), and correlation time describing its modulation (τ_{V}) were optimized through the best-fitting analysis of the experimental data to the IS relaxivity theory for the 3% CNCs + H_2O sample. The obtained parameters were then kept constant to fit the experimental data for the other CNC-containing samples because the relaxation dispersion trends for these samples are quite similar to each other. Hence the differences in the relaxivities for the CNC-containing systems could be explained alone in terms of the molar concentration (C) of dissolved metal (Fe) ions. The best-fitting curves estimated C = 0.11 mmol/L for the 3% CNCs + H_2O sample, which is lower than that obtained experimentally.

According to the obtained results, the main findings of this study can be summarized as:

- ^{1}H NMR relaxation data obtained herein revealed large differences between the dynamic behaviors of bulk water and water interacting with CNC−NaFh suspensions.
- It was determined that the proportion of CNCs governs the shape of the relaxation dispersion profiles in both the high- and low-frequency regions.
- The relaxivity of water protons in the CNC-based systems was markedly enhanced in the low-frequency domain, as water mobility was significantly reduced due to its interaction with CNC−NaFh suspensions.
- High-frequency bumps in the NMRD curves, dominated by the IS paramagnetic relaxation mechanism, were attributed to the interactions between Fe ions and water nuclei.
- At low concentrations (0.5 or 1.0%), NaFh particles turned out to have no noticeable influence on the T_1 relaxation behavior throughout the studied frequency range.

CONCLUSIONS

The present study aimed via PFG-NMR and NMR relaxometry to understand the molecular dynamics of water interacting with CNC−NaFh clay mineral nanocomposites and elucidate the role of these constrained environments in changing the dynamic behavior of solvent water. To that end, the longitudinal relaxation rates were measured for a broad range of Larmor frequencies, 10 kHz to 500 MHz. The relaxometry data indicated that the addition of a small concentration of CNCs to bulk H_2O is seen to not only significantly enhance the longitudinal relaxivity of the water protons but also to impart a pronounced frequency dependence on the low-frequency domain of the relaxation rate, which is not seen in isotropic H_2O. The NMRD profiles for bulk water and water with 1% clay were interpreted using a relaxation model that considered the sum of two relaxation contributions: local rotations and bulk-like translational diffusion. For the CNC-containing materials, on the contrary, two dominant relaxation processes were revealed to be attributed to the dynamics of confined water. The RMTD relaxation mechanism was found to be leading in the low- and intermediate-frequency domains, which stems from the interaction of water molecules with the CNC−NaFh surfaces. However, the high-frequency dispersions have been found to be mostly determined by the IS paramagnetic relaxation that is associated with the interaction of water protons with the paramagnetic entities. The observed paramagnetic relaxation effect was proportional to the concentration of CNCs. A remarkably high value of R_1 at low fields was obtained for the 3% CNCs + H_2O sample, for which the longitudinal relaxivity was found to increase up to 18-fold compared with that of the bulk water. This points to a global change in the water dynamics in the studied systems that is driven by the interaction of H_2O molecules with the CNC−NaFh particles.

■ AUTHOR INFORMATION

Corresponding Author

Anant Kumar − *Centro de Física e Engenharia de Materiais Avançados, Departamento de Física, Instituto Superior Técnico, Universidade de Lisboa, 1049-001 Lisboa, Portugal;* orcid.org/0000-0001-8427-5228; Email: anant.kumar@tecnico.ulisboa.pt

Authors

Carlos Cruz − *Centro de Física e Engenharia de Materiais Avançados, Departamento de Física, Instituto Superior Técnico, Universidade de Lisboa, 1049-001 Lisboa, Portugal*

João L. Figueirinhas − *Centro de Física e Engenharia de Materiais Avançados, Departamento de Física, Instituto Superior Técnico, Universidade de Lisboa, 1049-001 Lisboa, Portugal;* orcid.org/0000-0001-9254-1864

Pedro J. Sebastião − *Centro de Física e Engenharia de Materiais Avançados, Departamento de Física, Instituto Superior Técnico, Universidade de Lisboa, 1049-001 Lisboa, Portugal*

Ana C. Trindade − *Department of Physics, Norwegian University of Science and Technology, N-7492 Trondheim, Norway;* Present Address: Atlântica, Instituto Universitário, Fábrica da Pólvora de Barcarena, Barcarena 2730-036, Portugal

Susete N. Fernandes − *i3N/CENIMAT, Department of Materials Science, NOVA School of Science and Technology, NOVA University Lisbon, 2829-516 Caparica, Portugal;* orcid.org/0000-0002-7871-6717

Maria H. Godinho − *i3N/CENIMAT, Department of Materials Science, NOVA School of Science and Technology, NOVA University Lisbon, 2829-516 Caparica, Portugal*

Jon Otto Fossum − *Department of Physics, Norwegian University of Science and Technology, N-7492 Trondheim, Norway;* orcid.org/0000-0002-8952-303X

Complete contact information is available at: https://pubs.acs.org/10.1021/acs.jpcb.1c07331

Notes

The authors declare no competing financial interest.

■ ACKNOWLEDGMENTS

This work is cofinanced by FEDER, European funds, through the COMPETE 2020 POCI and PORL, National Funds, through FCT−Portuguese Foundation for Science and Technology and POR Lisboa2020, under the projects UID/CTM/04540/2013 (CeFEMA), UID/CTM/04540/2019 (CeFEMA), PIDDAC (POCI-01-0145-FEDER-007688, reference UIDB/50025/2020-2023), PTDC/CTM-REF/30529/2017 (NanoCell2SEC), M-ERA-NET2/0007/2016 (CellColor), and Action European Topology Interdisciplinary Action (EUTOPIA CA17139). Research was supported by NSF CMMI-1663041. We thank the Research Council of Norway − Nano2021 Program (250619 Graphene-NanoClay Systems). We acknowledge Florian Puchtler and Josef Breu from Lehrstuhl für Anorganische Chemie I, Universität Bayreuth, 95440 Bayreuth, Germany, for providing the sodium fluorohectorite material.

■ REFERENCES

(1) Camargo, P. H. C.; Satyanarayana, K. G.; Wypych, F. Nanocomposites: synthesis, structure, properties and new application opportunities. *Mater. Res.* **2009**, *12* (1), 1−39.

(2) Crosby, A. J.; Lee, J. Y.; et al. Polymer nanocomposites: the "nano" effect on mechanical properties. *Polym. Rev.* **2007**, *47* (2), 217−229.

(3) Dantas de Oliveira, A.; Augusto Goncalves Beatrice, C. Polymer nanocomposites with different types of nanofiller. *Nanocomposites-Recent Evolutions* **2019**, 103−104.

(4) Sahay, R.; Reddy, V. J.; Ramakrishna, S. Synthesis and applications of multifunctional composite nanomaterials. *Int. J. Mech. Mater. Eng.* **2014**, *9* (1), 25.

(5) Pavlidou, S.; Papaspyrides, C. D. A review on polymer−layered silicate nanocomposites. *Prog. Polym. Sci.* **2008**, *33* (12), 1119−1198.

(6) Blumstein, A. Polymerization of adsorbed monolayers. I. Preparation of the clay−polymer complex. *J. Polym. Sci., Part A: Gen. Pap.* **1965**, *3* (7), 2653−2664.

(7) Solomon, D. H.; Loft, B. C. Reactions catalyzed by minerals. Part III. The mechanism of spontaneous interlamellar polymerizations in aluminosilicates. *J. Appl. Polym. Sci.* **1968**, *12* (5), 1253−1262.

(8) Okada, A.; Kawasumi, M.; Usuki, A.; Kojima, Y.; Kurauchi, T.; Kamigaito, O. Nylon 6-clay hybrid. *Mater. Res. Soc. Symp. Proc.* **1989**, *171*, 45−50.

(9) Islam, M. M.; Khan, M. N.; Biswas, S.; Rabia Choudhury, T.; Haque, P.; U Rashid, T.; Mizanur Rahman, M. Preparation and characterization of bijoypur clay-crystalline cellulose composite for application as an adsorbent. *Adv. Mater. Sci.* **2017**, *2*, 1−7.

(10) Moon, R. J.; Martini, A.; Nairn, J.; Simonsen, J.; Youngblood, J. Cellulose nanomaterials review: structure, properties and nanocomposites. *Chem. Soc. Rev.* **2011**, *40* (7), 3941−3994.

(11) Newman, R. H.; Hemmingson, J. A. Carbon-13 NMR distinction between categories of molecular order and disorder in cellulose. *Cellulose* **1995**, *2* (2), 95−110.

(12) Islam, M. S.; Chen, L.; Sisler, J.; Tam, K. C. Cellulose nanocrystal (CNC)−inorganic hybrid systems: synthesis, properties and applications. *J. Mater. Chem. B* **2018**, *6* (6), 864−883.

(13) Schlesinger, M.; Hamad, W. Y.; MacLachlan, M. J. Optically tunable chiral nematic mesoporous cellulose films. *Soft Matter* **2015**, *11* (23), 4686−4694.

(14) Beck, S.; Bouchard, J.; Berry, R. Controlling the reflection wavelength of iridescent solid films of nanocrystalline cellulose. *Biomacromolecules* **2011**, *12* (1), 167−172.

(15) Fernandes, S. N.; Geng, Y.; Vignolini, S.; Glover, B. J.; Trindade, A. C.; Canejo, J. P.; Almeida, P. L.; Brogueira, P.; Godinho, M. H. Structural color and iridescence in transparent sheared cellulosic films. *Macromol. Chem. Phys.* **2013**, *214* (1), 25−32.

(16) Bardet, R.; Belgacem, N.; Bras, J. Flexibility and color monitoring of cellulose nanocrystal iridescent solid films using

anionic or neutral polymers. *ACS Appl. Mater. Interfaces* **2015**, *7* (7), 4010−4018.

(17) Wang, P. X.; Hamad, W. Y.; MacLachlan, M. J. Structure and transformation of tactoids in cellulose nanocrystal suspensions. *Nat. Commun.* **2016**, *7* (1), 1−8.

(18) McCormick, C. Nanocellulose steps up on stage. *Pulp Paper-Canada* **2010**, *111*, 15−16.

(19) Arora, A.; Padua, G. W. Nanocomposites in food packaging. *J. Food Sci.* **2010**, *75* (1), R43−R49.

(20) Müller, K.; Bugnicourt, E.; Latorre, M.; Jorda, M.; Echegoyen Sanz, Y.; Lagaron, J. M.; Miesbauer, O.; Bianchin, A.; Hankin, S.; Bölz, U.; et al. Review on the processing and properties of polymer nanocomposites and nanocoatings and their applications in the packaging, automotive and solar energy fields. *Nanomaterials* **2017**, *7* (4), 74.

(21) Michels-Brito, P. H.; Malfatti-Gasperini, A.; Mayr, L.; Puentes-Martinez, X.; Tenório, R. P.; Wagner, D. R.; Knudsen, K. D.; Araki, K.; Oliveira, R. G.; Breu, J.; et al. Unmodified Clay Nanosheets at the Air−Water Interface. *Langmuir* **2021**, *37* (1), 160−170.

(22) Hansen, E. L.; Hemmen, H.; Fonseca, D. D. M.; Coutant, C.; Knudsen, K. D.; Plivelic, T. S.; Bonn, D.; Fossum, J. O. Swelling transition of a clay induced by heating. *Sci. Rep.* **2012**, *2*, 618.

(23) Stöter, M.; Rosenfeldt, S.; Breu, J. Tunable exfoliation of synthetic clays. *Annu. Rev. Mater. Res.* **2015**, *45*, 129−151.

(24) Calabi Floody, M.; Theng, B. K. G.; Reyes, P.; Mora, M. L. Natural nanoclays: applications and future trends−a Chilean perspective. *Clay Miner.* **2009**, *44* (2), 161−176.

(25) Patel, H. A.; Somani, R. S.; Bajaj, H. C.; Jasra, R. V. Nanoclays for polymer nanocomposites, paints, inks, greases and cosmetics formulations, drug delivery vehicle and waste water treatment. *Bull. Mater. Sci.* **2006**, *29* (2), 133−145.

(26) Albdiry, M. T.; Yousif, B. F.; Ku, H.; Lau, K. T. A critical review on the manufacturing processes in relation to the properties of nanoclay/polymer composites. *J. Compos. Mater.* **2013**, *47* (9), 1093−1115.

(27) Choudhury, A.; Bhowmick, A. K.; Ong, C. Novel role of polymer−solvent and clay−solvent interaction parameters on the thermal, mechanical and optical properties of polymer nanocomposites. *Polymer* **2009**, *50* (1), 201−210.

(28) Sung, K.; Nakagawa, S.; Yoshie, N. Fabrication of water-resistant nacre-like polymer/clay nanocomposites via in situ polymerization. *ACS Omega* **2017**, *2* (11), 8475−8482.

(29) Stöter, M.; Kunz, D. A.; Schmidt, M.; Hirsemann, D.; Kalo, H.; Putz, B.; Senker, J.; Breu, J. Nanoplatelets of sodium hectorite showing aspect ratios of≍ 20 000 and superior purity. *Langmuir* **2013**, *29* (4), 1280−1285.

(30) Saraiva, D. V.; Chagas, R.; Abreu, B. M. D.; Gouveia, C. N.; Silva, P. E.; Godinho, M. H.; Fernandes, S. N. Flexible and structural coloured composite films from cellulose nanocrystals/hydroxypropyl cellulose lyotropic suspensions. *Crystals* **2020**, *10* (2), 122.

(31) Dong, X. M.; Kimura, T.; Revol, J. F.; Gray, D. G. Effects of ionic strength on the isotropic- chiral nematic phase transition of suspensions of cellulose crystallites. *Langmuir* **1996**, *12* (8), 2076−2082.

(32) Trindade, A. C.; Carreto, M.; Helgesen, G.; Knudsen, K. D.; Puchtler, F.; Breu, J.; Fernandes, S.; Godinho, M. H.; Fossum, J. O. Photonic composite materials from cellulose nanorods and clay nanolayers. *Eur. Phys. J.: Spec. Top.* **2020**, *229* (17), 2741−2755.

(33) Hamad, W. Y.; Hu, T. Q. Structure−process−yield interrelations in nanocrystalline cellulose extraction. *Can. J. Chem. Eng.* **2010**, *88* (3), 392−402.

(34) Fukushima, E. *Experimental Pulse NMR: A Nuts and Bolts Approach*; CRC Press, 2018.

(35) Mesquita Sousa, D.; Domingos Marques, G.; Manuel Cascais, J.; Jose Sebastiao, P. Desktop fast-field cycling nuclear magnetic resonance relaxometer. *Solid State Nucl. Magn. Reson.* **2010**, *38* (1), 36−43.

(36) Kimmich, R. *NMR: Tomography, Diffusometry, Relaxometry*; Springer Science & Business Media, 2012.

(37) Price, W. S. Pulsed-field gradient nuclear magnetic resonance as a tool for studying translational diffusion: Part 1. Basic theory. *Concepts Magn. Reson.* **1997**, *9* (5), 299−336.

(38) Price, W. S. Pulsed-field gradient nuclear magnetic resonance as a tool for studying translational diffusion: Part II. *Concepts Magn. Reson.* **1998**, *10* (4), 197−237.

(39) Sebastiao, P. J The art of model fitting to experimental results. *Eur. J. Phys.* **2014**, *35*, 015017.

(40) Bloembergen, N.; Purcell, E. M.; Pound, R. V. Relaxation effects in nuclear magnetic resonance absorption. *Phys. Rev.* **1948**, *73* (7), 679.

(41) Torrey, H. C. Nuclear spin relaxation by translational diffusion. *Phys. Rev.* **1953**, *92* (4), 962.

(42) Solomon, I. Relaxation processes in a system of two spins. *Phys. Rev.* **1955**, *99* (2), 559.

(43) Bloembergen, N. Proton relaxation times in paramagnetic solutions. *J. Chem. Phys.* **1957**, *27* (2), 572−573.

(44) Bloembergen, N.; Morgan, L. O. Proton relaxation times in paramagnetic solutions. Effects of electron spin relaxation. *J. Chem. Phys.* **1961**, *34* (3), 842−850.

(45) *Cancer Imaging: Lung and Breast Carcinomas*; Hayat, M. A., Ed.; Elsevier Science & Technology, 2008; Vol. *1*.

(46) *Contrast Agents for MRI: Experimental Methods*; Pierre, V. C., Allen, M. J., Eds.; Royal Society of Chemistry, 2017; Vol. *13*.

(47) Hwang, L. P.; Freed, J. H. Dynamic effects of pair correlation functions on spin relaxation by translational diffusion in liquids. *J. Chem. Phys.* **1975**, *63* (9), 4017−4025.

(48) Freed, J. H. Dynamic effects of pair correlation functions on spin relaxation by translational diffusion in liquids. II. Finite jumps and independent T1 processes. *J. Chem. Phys.* **1978**, *68* (9), 4034−4037.

(49) Zavada, T.; Kimmich, R. The anomalous adsorbate dynamics at surfaces in porous media studied by nuclear magnetic resonance methods. The orientational structure factor and Lévy walks. *J. Chem. Phys.* **1998**, *109* (16), 6929−6939.

(50) Kimmich, R. *Principles of Soft-Matter Dynamics: Basic Theories, Non-Invasive Methods, Mesoscopic Aspects*; Springer Science & Business Media, 2012.

(51) Kowalczuk, J.; Rachocki, A.; Bielejewski, M.; Tritt-Goc, J. Effect of gel matrix confinement on the solvent dynamics in supramolecular gels. *J. Colloid Interface Sci.* **2016**, *472*, 60−68.

(52) Vilfan, M.; Apih, T.; Sebastiao, P. J.; Lahajnar, G.; Zumer, S. Liquid crystal 8CB in random porous glass: NMR relaxometry study of molecular diffusion and director fluctuations. *Phys. Rev. E* **2007**, *76* (5), 051708.